ADVANCED ELECTRONIC MATERIALS Open Access
www.advelectronicmat.de

Harnessing Earth-Abundant Lead-Free Halide Perovskite for Resistive Switching Memory and Neuromorphic Computing

Zijian Feng, Jiyun Kim, Jie Min, Peiyuan Guan, Shuo Zhang, Xinwei Guan, Tingting Mei, Tianxu Huang, Chun-Ho Lin, Long Hu,* Fandi Chen,* Zhi Li, Jiabao Yi, Tom Wu, and Dewei Chu**

Non-volatile memories are expected to revolutionize a wide range of information technologies, but their manufacturing cost is one of the top concerns researchers must address. This study presents a 1D lead-free halide perovskite K_2CuBr_3, as a novel material candidate for the resistive switching (RS) devices, which features only earth-abundant elements, K, Cu, and Br. To the knowledge, this material is the first low-dimensional halide perovskite with exceptionally low production costs and minimal environmental impact. Owing to the unique 1D carrier transport along the Cu—Br networks, the K_2CuBr_3 RS device exhibits excellent bipolar switching behavior, with an On/Off window of 10^5 and a retention time of over 1000 s. The K_2CuBr_3 RS devices can also act as artificial synapses to transmit various forms of synaptic plasticities, and their integration into a perceptron artificial neural network can deliver a high algorithm accuracy of 93% for image recognition. Overall, this study underscores the promising attributes of K_2CuBr_3 for the future development of memory storage and neuromorphic computing, leveraging its distinct material properties and economic benefits.

1. Introduction

The rapid development in integrated circuits (ICs) and artificial intelligence (AI) have significantly facilitated the level of human life. However, the physical limitations imposed by Moore's Law and the von Neumann bottleneck have driven researchers to pursue alternative memory materials and device architectures to sustain technological growth. Resistive switching (RS) memory, characterized by its ability to reversibly switch between high resistance state (HRS) and low resistance state (LRS), has become pivotal in data storage technology. Compared to conventional silicon-based non-volatile memory, RS memory is noted for its faster response speed, high write-erase cycle endurance, lower power consumption, and smaller cell size.[1] Moreover, the meticulous modulation of resistance between HRS and LRS under electrical pulse stimuli is similar to the behavior of a biological synapse, facilitating applications in neuromorphic computing devices, including artificial synapse,[2] nociceptor,[3,4] photo-synapse[5] and artificial neural network (ANN).[6–8] Neuromorphic computing based on resistive switching devices has demonstrated remarkable potential for enabling highly efficient and low-power computational systems. These devices excel in handling complex, parallel, and spatiotemporal data processing tasks, essential for applications in robotics, autonomous systems, and event-driven artificial intelligence. Their seamless integration with network-on-chip architectures and compatibility with complementary metal-oxide semiconductor technologies further positions them as a transformative technology for future intelligent systems.[9]

Z. Feng, J. Kim, J. Min, P. Guan, S. Zhang, T. Mei, T. Huang, C.-H. Lin, L. Hu, F. Chen, Z. Li, T. Wu, D. Chu
School of Materials Science and Engineering
University of New South Wales
Sydney, NSW 2052, Australia
E-mail: chun-ho.lin@unsw.edu.au; long.hu@unsw.edu.au; fandi.chen@unsw.edu.au; d.chu@unsw.edu.au

X. Guan, J. Yi
Global Innovative Centre for Advanced Nanomaterials
School of Engineering
College of Engineering
Science and Environment
The University of Newcastle
Callaghan, NSW 2308, Australia

X. Guan
School of Science
RMIT University
Melbourne, VIC 3000, Australia

T. Wu
Department of Applied Physics
The Hong Kong Polytechnic University
Kowloon, Hong Kong 999077, China

The ORCID identification number(s) for the author(s) of this article can be found under https://doi.org/10.1002/aelm.202400804

DOI: 10.1002/aelm.202400804

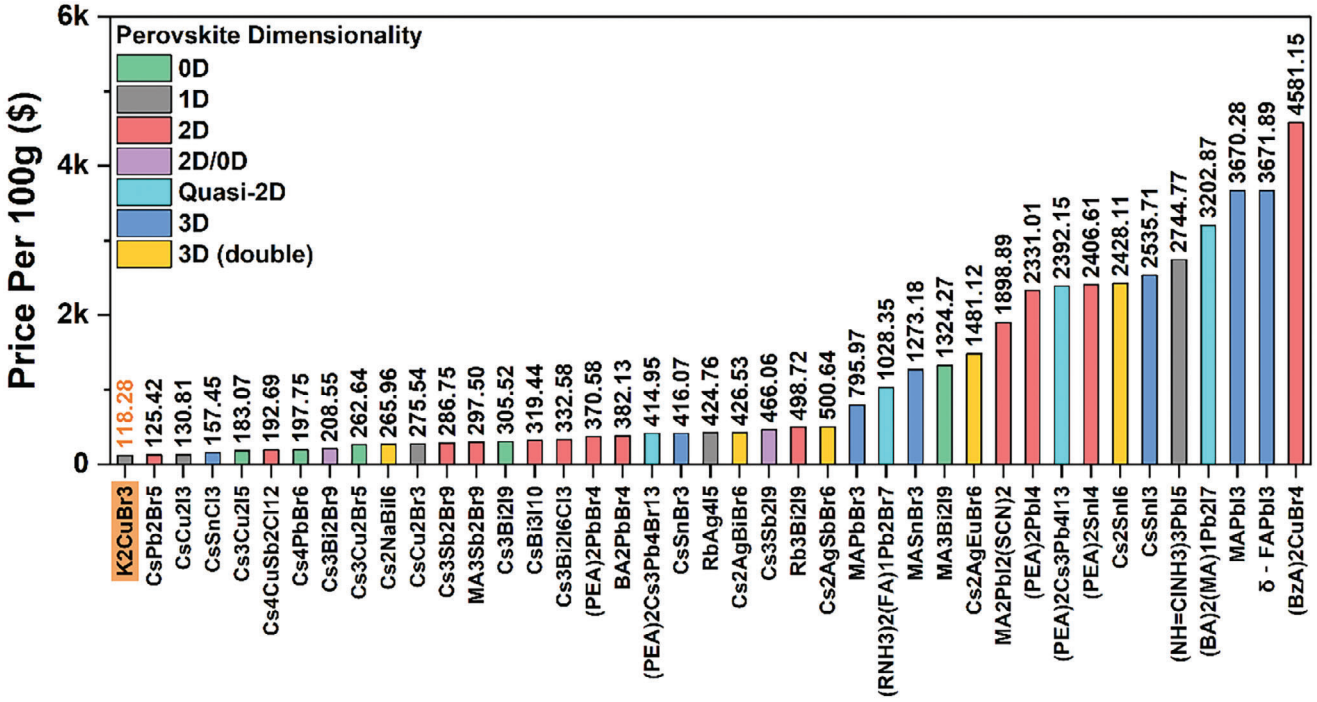

Figure 1. Price of precursors (US dollar) used in fabricating 100 grams of perovskite, purity ≥99%. Data was collected from Sigma in November 2023.

Recently, halide perovskites with distinctive crystal structures have shown great promise in RS applications. Their soft lattices feature low-energy barriers[10] that allow the migration of halogen vacancies or mobile ions to form conductive filaments within the lattice, which is the key mechanism for the RS phenomenon.[11] Additionally, the fabrication of perovskite semiconductors avoids typical high-temperature processes, thereby significantly reducing energy consumption, manufacturing complexity, and cost.[12,13] Due to the wide availability of A-site cations (which connect the individual perovskite B-X network), B-site cations, and X anions (forming the B-X metal halide network) to fit with perovskite structure, it allows effective tuning of perovskite properties to suit a variety of applications. This includes the ability to modify their molecular dimensionalities from 0D to 3D. For example, lead-based 3D perovskites have garnered the most interest due to their lone-pair Pb 6s orbit, inactive Pb 6p orbit, and strong spin-orbit coupling (SOC),[14,15] contributing to an ideal bandgap and excellent charge transport for solar applications.

However, lead-based perovskite is also problematic, primarily concerning health and environmental risks associated with lead.[16] As an alternative, Sn-based 3D perovskites have been studied since it has an electron configuration similar to lead,[17] however, Sn (II) ion can be easily oxidized into Sn (IV),[18] leading to deteriorated device performance. As a result, recent research has focused on lower-dimensional, lead-free perovskites, including 2D, 1D, and 0D molecular structures.[19] Elements such as Bi, Sb, and Cu have been utilized to construct low-dimensional structures,[20] where the individual 2D, 1D, or 0D metal halide building blocks are separated from each other by spacer cations, and the perovskites can exhibit the unique intrinsic properties of the individual building blocks. Due to the isolated nature of molecular low-dimensional perovskites, the electronic carriers predominantly move within the confined metal halide networks, leading to lower intrinsic conductivity than typical 3D perovskites.[21] This can significantly decrease the OFF-state current for memory/neuromorphic devices, allowing a larger On/Off ratio and reducing energy consumption, together with its less-toxic nature and desirable soft lattices, lead-free low-dimensional perovskites are considered superior candidates for memristor applications.[22]

In this work, we introduce 1D K_2CuBr_3 thin films for RS memory and artificial synapse for the first time. Due to the earth-abundant nature, the precursor material cost for K_2CuBr_3 is found to be the lowest among all the family of halide perovskite memories reported so far. As illustrated in **Figure 1**, based on market price, the cost of precursors for fabricating 100 grams of K_2CuBr_3 is only 118.28 US$/100 g, which is significantly lower than that of other 1D halide perovskites, and shows a huge cost advantage compared to conventional organic-inorganic halide perovskites and lead-based perovskites, which typically exceed 1000 US$/100g. In addition, the environmental impact can also be minimized compared to conventional halide perovskites, as K_2CuBr_3 is derived from widely available, non-toxic elements, making it a more environmentally friendly alternative. The RS devices based on thermally evaporated K_2CuBr_3 thin films exhibit desirable digital switching behavior with a high On/Off memory window of over 10^5 and a retention time of over 1000 s. The K_2CuBr_3 memristor devices can also conduct different artificial synapse functions, including short/long term potentiation (STP/LTP), pair-pulse facilitation (PPF), and synaptic number/intensity/rate/duration dependent plasticities (SNDP, SIDP, SRDP, SDDP). Overall, the results demonstrated here advance the development of low-cost, lead-free K_2CuBr_3 for memory

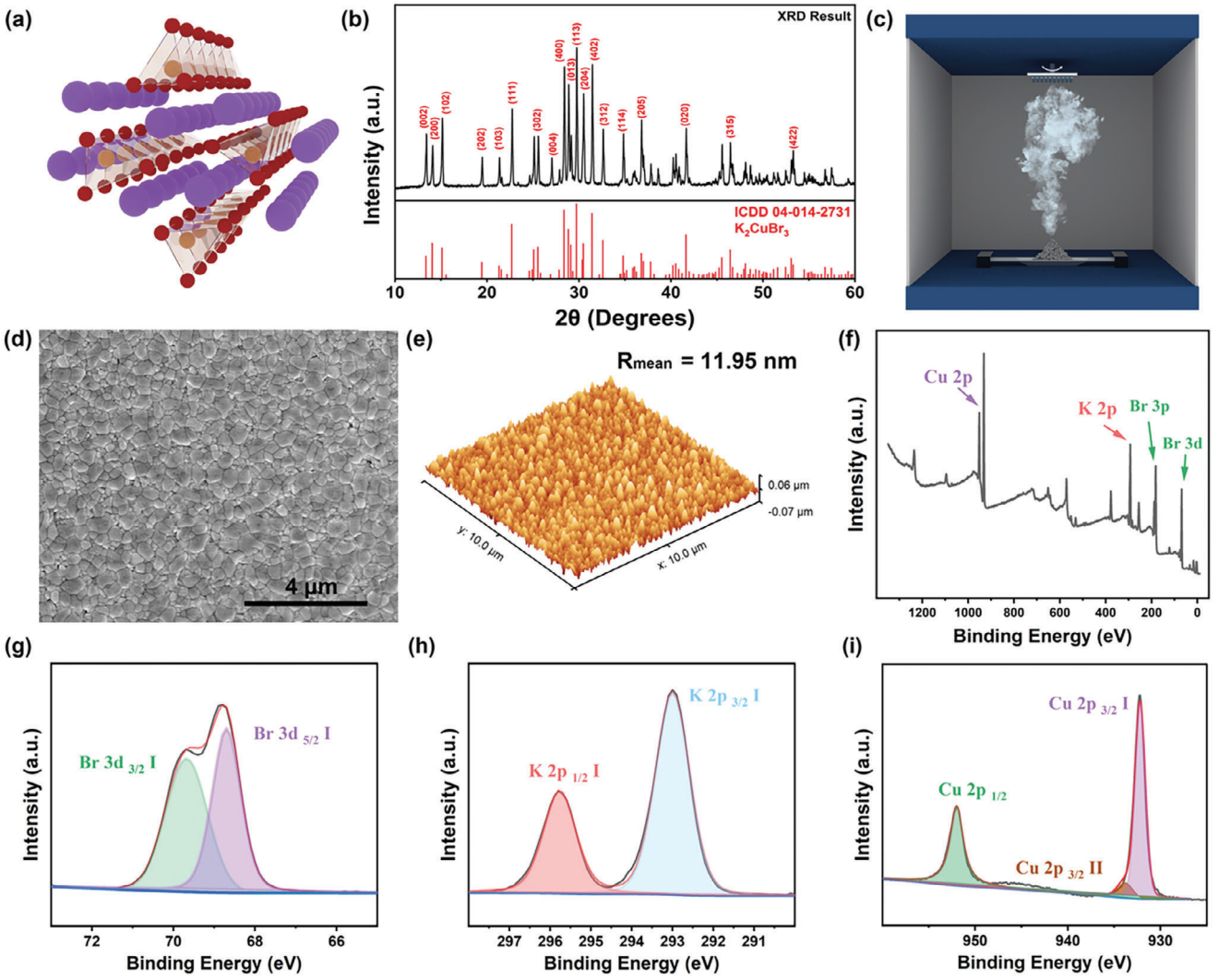

Figure 2. a) Schematic illustration of the K_2CuBr_3 crystal structure. b) XRD spectrum of synthesized K_2CuBr_3 powder compared to reference pattern ICDD 04-014-2731. c) Schematic illustration of VTE thin film deposition. d) SEM image of K_2CuBr_3 film surface. e) AFM examination of K_2CuBr_3 surface. f) XPS full spectrum of K_2CuBr_3 film. XPS core spectra of K_2CuBr_3 film at g) Br-3d, h) K-2p, and i) Cu-2p regions.

storage and neuromorphic computing, leveraging its unique material properties and economic benefits.

2. Results and Discussion

The crystal structure of K_2CuBr_3 is demonstrated in **Figure** 2a. The copper and bromide atoms are arranged to form the Cu—Br tetrahedron networks, which are connected to each other by sharing corners with neighboring tetrahedrons and forming a 1D Cu—Br chain. Potassium atoms are positioned between Cu—Br chains to separate them, thus contributing to the overall formation of the 1D perovskite structure. The K_2CuBr_3 powders were first prepared by a solid-state reaction (see Experimental Section). The prepared K_2CuBr_3 powder is examined by powder X-ray diffraction (XRD) measurements, as shown in Figure 2b, which shows multiple sharp peaks that match the reference record for 1D K_2CuBr_3 (ICDD 04-014-2731). The 1D Cu—Br tetrahedron networks can endow K_2CuBr_3 with anisotropic carrier transport property. Previous reports on perovskite dimensionality research and density functional theory (DFT) calculation have revealed that the low-dimensional 1D structure can facilitate ion migration due to the anisotropic migration barrier.[23,24] This can potentially reduce the SET voltage in RS devices, thus decreasing energy consumption. In this work, the K_2CuBr_3 thin films were fabricated from the powders using the single-source vacuum thermal evaporation (VTE) method, which enables simple control, large-area, and high-throughput fabrication, as shown in the schematic diagram **Figure** 2c. Previous studies reported that the appearance of KBr/CuBr impurities in fabricating K_2CuBr_3 is possible,[25,26] which is also supported by the XRD pattern (Figure S1, Supporting Information).

To investigate the quality of thin films, scanning electron microscopy (SEM) was used to examine the surface morphology. As depicted in Figure 2d, the K_2CuBr_3 film formed by VTE deposition shows a smooth and continuous surface with densely packed grains and an average grain size of ≈300 nm. The K_2CuBr_3

surface roughness was also investigated by atomic force microscope (AFM), obtaining a mean roughness of 11.95 nm (Figure 2e). These characteristics indicate that the K_2CuBr_3 film is smooth and dense without significant pinholes, which is beneficial for RS device application.

X-ray photoelectron spectroscopy (XPS) has been employed to further study the K_2CuBr_3 film. As depicted in Figure 2f, the peaks from Cu, K, and Br can be clearly observed in the overall survey of K_2CuBr_3. The Br-3d spectrum in Figure 2g, reveals two signals at 69.7 and 68.7 eV, which correspond to the Br-$3d_{3/2}$[27] and Br-$3d_{5/2}$[28] orbit, respectively. Figure 2h displays the peak at 295.8 and 292.8 eV, which matches the K-$2p_{1/2}$[29] and K-$2p_{3/2}$[30] orbits in the K^+ ion. The Cu-2p spectrum in Figure 2i features the Cu-$2p_{1/2}$ peak at a binding energy of 952.0 eV[31] and highlights a strong signal at 932.2 eV along with a weaker signal at 933.7 eV, both indicative of the Cu-$2p_{3/2}$ orbit,[32,33] suggesting the primary presence of monovalent Cu^+.[34] The atomic ratio analysis derived from the XPS survey reveals that the ratio of K, Cu, and Br is ≈2:1:3 (Table S1, Supporting Information), which matches the desired ratio of the K_2CuBr_3. Thermogravimetric analysis (TGA) and differential scanning calorimetry (DSC) measurements were also conducted to examine the properties of K_2CuBr_3 (Figures S2 and S3, Supporting Information). The TGA spectrum indicates that K_2CuBr_3 exhibits no noticeable weight loss up to 650 °C, while the DSC data reveals a pronounced peak at 244.2 C. The observed thermal event can be attributed to the melting point of K_2CuBr_3, as suggested by the reported KBr–CuBr phase diagram.[25]

Our synthesized K_2CuBr_3 thin films can exhibit strong blue light photoluminescence (PL) under a UV lamp (**Figure 3a**). To further investigate its PL property, both PL and photoluminescence excitation (PLE) spectra were tested as shown in Figure 3b. PL spectrum shows the peak location at 379 nm, indicating an emission within the blue range, which is consistent with the result in Figure 3a. The PLE spectrum reveals a maximum excitation at 294 nm, with a large Stokes shift of 0.94 eV compared to the PL peak, implying the occurrence of self-trapped exciton (STE) emission in K_2CuBr_3 crystals.[26,35–37] The formation of STEs has been reported in various 1D perovskites owing to strong electron-phonon coupling within the lattice distortion field, which can create covalent bonds in the excited state that are absent in the ground state.[38] The mechanism of STE emission is illustrated in Figure 3c. Upon photoexcitation, electrons are initially excited to free-exciton states. These free excitons then rapidly relax into STE states and the decay from these trapped centers leads to the STE emission with a longer wavelength than its excitation peak. In 1D K_2CuBr_3, the configuration variation of Cu—Br bonds under excitation can lead to Jahn–Teller distortions,[39] which serve as centers for STE formation. These dynamic second-order Jahn–Teller instability may enhance ion migration in the perovskite,[40] which can potentially benefit RS device that relies on ion movement. These free excitons then rapidly relax into STE states and the decay from these trapped centers leads to the STE emission with a longer wavelength than its excitation peak. In 1D K_2CuBr_3, the configuration variation of Cu—Br bonds under excitation can lead to Jahn–Teller distortions,[39] which serve as centers for STE formation. These dynamic second-order Jahn–Teller instability may enhance ion migration in the perovskite,[40] which can potentially benefit RS device that relies on ion movement. From previous studies, the Jahn-Teller distortion induces local lattice distortions by elongating certain bonds, reducing the symmetry, as well as the system energy. This local lattice deformation enhances electron-phonon coupling, leading to the localization of charge carriers and stabilizing the STE.[41–43] The Jahn–Teller distortions and associated polaron formation create localized regions of strain and defect states, which can serve as pathways for ions to migrate under an external electric field.[40] We also examined the Raman spectrum of K_2CuBr_3 (Figure S4, Supporting Information), in which the two peaks at 130 and 148 eV can be attributed to the vibration of the Cu—Br bonds. According to the previous report,[39] these two vibration modes may contribute to the electron-phonon coupling, endowing K_2CuBr_3 with the distinct STE property.

To investigate the band structure of K_2CuBr_3, UV–vis spectroscopy and Ultraviolet Photoelectron Spectroscopy (UPS) are employed in this study. The UV–vis spectrum of K_2CuBr_3 demonstrates its reflectance across 200 to 800 nm wavelength range (Figure S5, Supporting Information). Based on the result, the bandgap width is calculated using the Kubelka-Munk equation shown as follows:[44]

$$F = \frac{K}{S} = \frac{(1-R)^2}{2R} \tag{1}$$

where K is the absorption coefficient, S is the scattering coefficient, and R refers to the reflectance. As illustrated in Figure 3d, the calculated Tauc plot revealed a bandgap of 3.77 eV for K_2CuBr_3. To further clarify the band structure, UPS spectra in the cutoff and valance band regions were obtained (Figure 3e,f), and the valance band maximum (VBM) and fermi level (E_F) position of K_2CuBr_3 were calculated using the following equations:[45,46]

$$E_F = 21.22 - E_{cutoff} \tag{2}$$

$$VBM = 21.22 - \left(E_{cutoff} - E_{onset}\right) \tag{3}$$

where 21.22 eV is the excitation photon energy, E_{cutoff} and E_{onset} refer to the spectrum tangent in the cutoff region and valance band region, respectively. The E_F position and VBM are calculated to be −3.67 and −5.22 eV, respectively, and together with the Tauc plot obtained bandgap, the conduction band minimum (CBM) is determined to be −1.45 eV. The overall band structure of K_2CuBr_3, depicted in Figure 3g, indicates a slight p-type behavior, consistent with the usually observed p-type characteristics in Cu-based hybrid semiconductors.[47] When selecting a metal electrode for constructing a K_2CuBr_3-based RS device, the Schottky barrier height, determined by the difference between the VBM of the semiconductor and the metal's work function, should be considered.[48] For K_2CuBr_3 (VBM: −5.22 eV), the Ag (work function: −4.2 eV) electrode can be a better candidate than Au (work function: −5.1 eV) since larger Schottky barriers are preferred for RS devices, which can reduce the OFF state current and the associated energy consumption.

In Figure 3h, the DFT simulated density of state (DOS) demonstrates that the electron orbitals from copper predominantly contribute to the valence band structure. On the other hand, the electron orbit from bromide has a weak contribution to the band structure when hybridized with Cu orbit. Furthermore, it is found

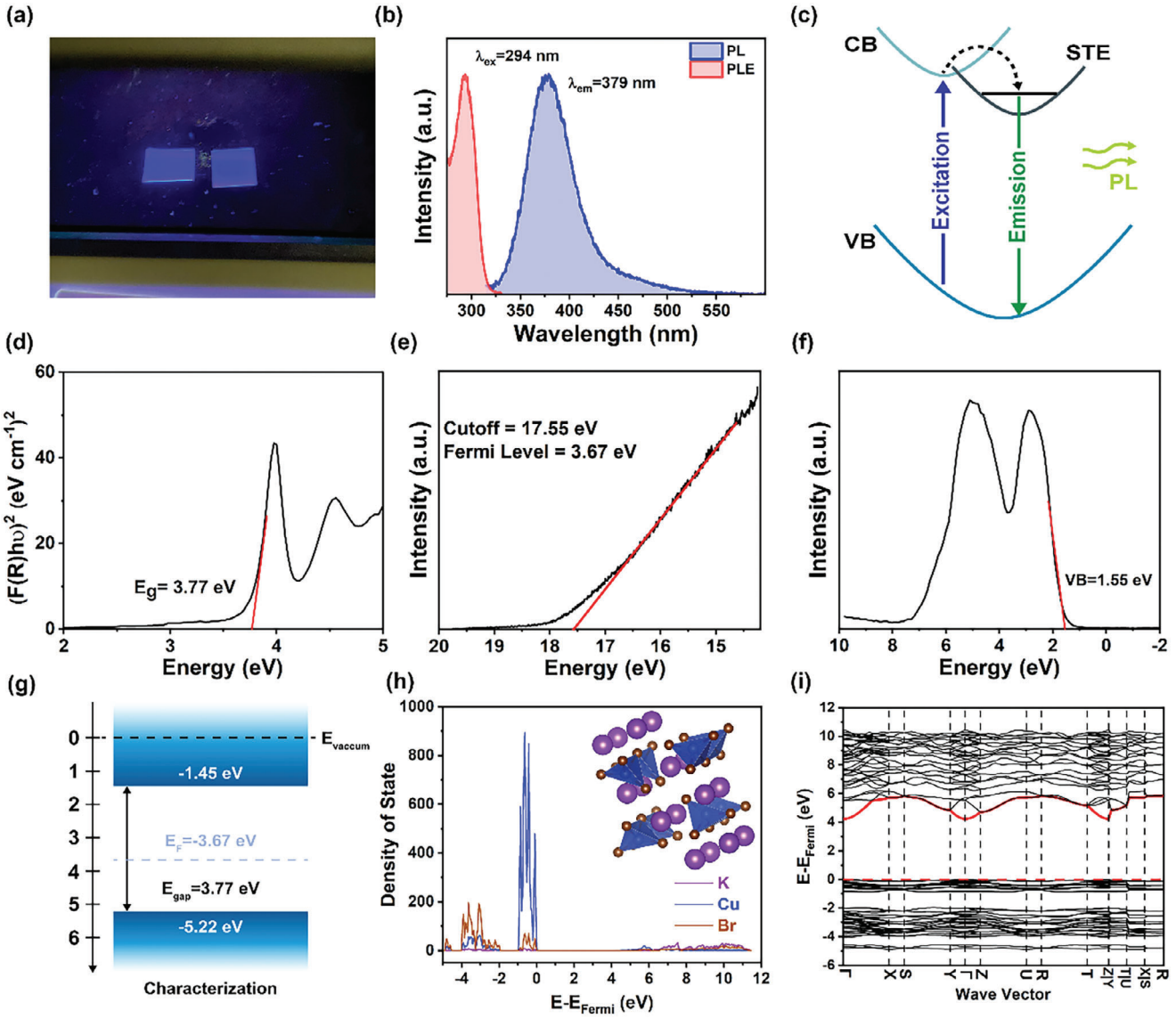

Figure 3. a) Photograph of K_2CuBr_3 thin films under UV excitation. b) PL and PLE spectra of K_2CuBr_3. c) Schematic diagram of STE emission mechanism. d) Tauc plot of K_2CuBr_3, calculated from UV–vis results with Kubelka-Munk function. UPS spectra of K_2CuBr_3 in the e) cutoff region and f) valance band region. g) Schematic diagram of measured K_2CuBr_3 band structure. h) DOS plot and i) band structure of K_2CuBr_3 calculated by DFT simulation.

that the potassium ions have minimal effect on the band structure, which is consistent with the molecular structure of K_2CuBr_3 crystals, where the potassium ions only separate the 1D Cu-Br chains.[39] The Brillouin zone shown in Figure 3i demonstrates the bandgap calculated with hybrid functional b3lyp, ending with a simulated value of 4.23 eV at the wavevector Γ point. The minimal dispersion of the VBM position suggests that the carrier's effective mass is substantial. Consequently, carriers are likely to be confined in the 1D Cu-Br chains.[39] The confined 1D carrier transport theoretically can lead to lower Off-state current than typical perovskites, which is beneficial for the digital/neuromorphic switching devices by enhancing the On/Off ratio and reducing energy consumption.

Our K_2CuBr_3 RS device adopted a typical metal-semiconductor-metal (MSM) layered structure, in which the ITO and Ag serve as the bottom and top contacts, respectively, as shown in the illustration in **Figure** 4a and photograph in Figure S6 (Supporting Information). The cross-sectional SEM image of the device confirms the MSM structure with 100 nm Ag top electrode (TE), ≈300 nm K_2CuBr_3 functional layer, and ITO glass bottom electrode (BE, Figure 4b). The RS property of the Ag/K_2CuBr_3/ITO device is shown in Figure 4c, in which a significant hysteresis loop was recorded when applying a DC voltage bias sweep (0 V→0.4 V→0 V→-0.4 V→0 V) on the silver TE, demonstrating a bipolar resistive switching behavior with a large memory window. During the voltage sweep from 0 to 0.4 V, the device was in HRS with a small current of 1 nA flowing through the device. When the applied voltage approached 0.3 V, the recorded current increased dramatically to the magnitude of 10^{-4} A, demonstrating the resistive switching

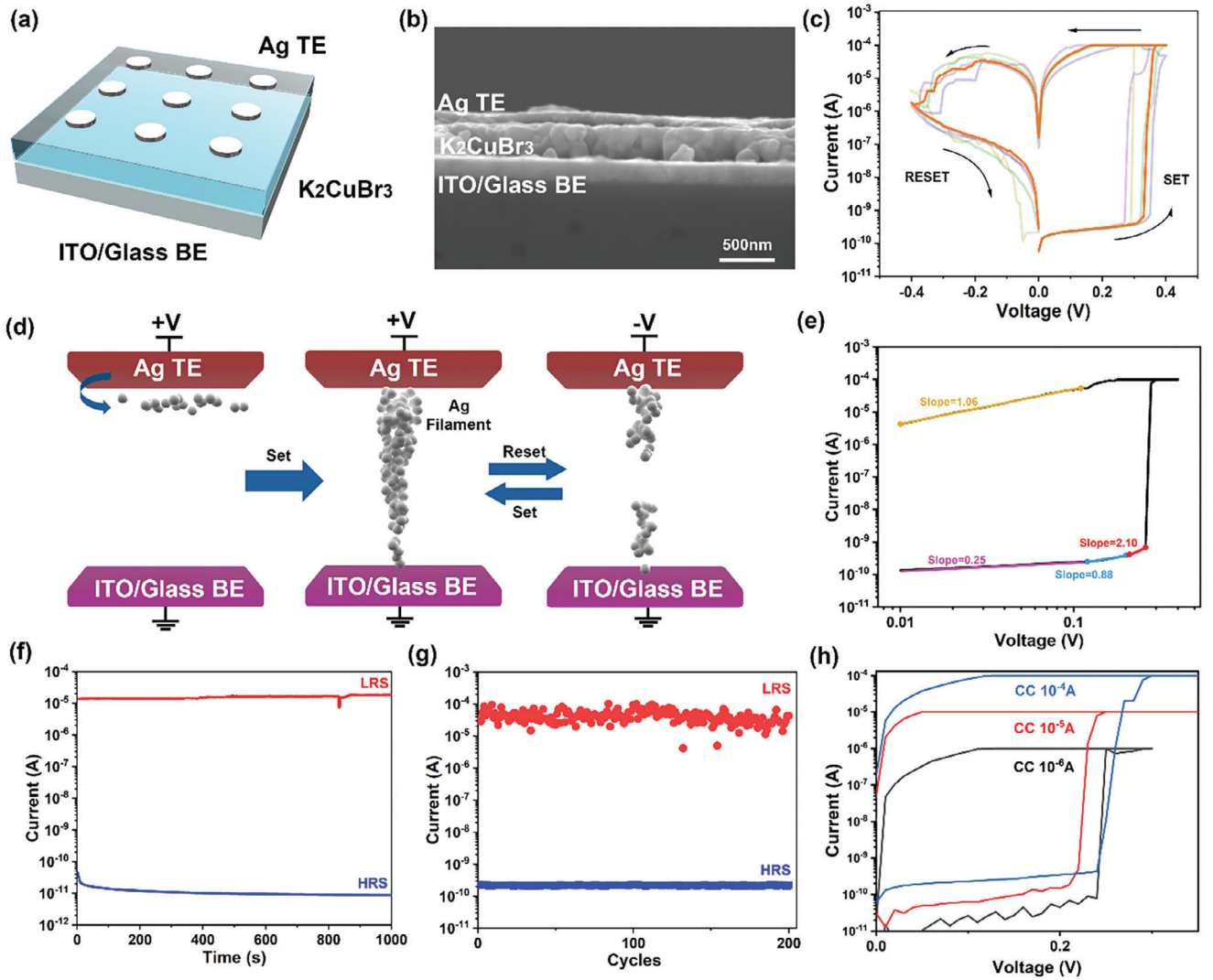

Figure 4. a) Schematic diagram and b) cross-sectional SEM image of Ag/K_2CuBr_3/ITO RS device. c) *I–V* characteristics of K_2CuBr_3 RS device under voltage bias sweep (0V→0.4V→0V→-0.4V→0 V). d) Schematic diagram showing the electrochemical metallization mechanism of RS behavior. e) Log I versus log V sweep curve of K_2CuBr_3 RS device. f) Retention test and g) cyclic endurance test of the K_2CuBr_3 RS device. h) The effect of different compliance current (CC) settings during the RS testing.

to the LRS, namely the "SET" process of the memory device. The device remained in LRS when the voltage swept from 0.4 to 0 V. During the sweep from 0 to −0.4 V, the recorded current decreased rapidly when approaching −0.2 V, in which the device underwent the "RESET" process and switched back to the HRS. The On/Off ratio of the device can reach 10^5 between HRS and LRS, demonstrating an excellent property in resistive switching applications. Figure S7 (Supporting Information) shows the statistical distribution of measured SET and RESET voltages, in which the average SET voltage is 0.317 V and the RESET voltage is −0.289 V. Furthermore, the switching time from HRS to LRS is estimated to be 0.6 s, while the switching time from LRS back to HRS is ranging from 0.3 to 0.75 s, as shown in Figure S8 (Supporting Information). In this study, the K_2CuBr_3 RS device is fabricated using a shadow mask with an array configuration. Figure S9 (Supporting Information) shows the *I–V* tests of 10 devices in an array, demonstrating a consistent RS behavior. Figure 4d is a schematic diagram that demonstrates the RS mechanism. When an external positive voltage is applied, the Ag TE can undergo oxidation and produce mobile Ag ions migrating into the vacancies of the perovskite layer, as reported previously.[49] In this study, we performed the *I–V* experiments with a probe station under vacuum conditions. Therefore, the redox reaction between perovskite and Ag under external voltage bias is responsible for the generation of mobile Ag ions instead of oxygen-related oxidation. With a further increase in voltage, the mobile Ag ions are driven to form a conductive filament through the perovskite layer, thereby switching the resistance of the device to LRS. This conductive filament can rupture when a negative voltage is applied, causing the device to switch back to the HRS. To further confirm the filament-type mechanism of our RS devices instead of interface-type, we changed the size of the

Table 1. Performance summary of 1D halide perovskite-based RS devices in the literature and this work.

Perovskite	On/Off ratio	Retention	Cycle	SET/RESET Voltage	Lead-Free	Refs.
$(Im)PbI_3$	10^6	10^4 s	1000	0.2 V/-0.2 V	No	[24]
$(NH=ClNH_3)_3PbI_5$	10^3	10^4 s	<200	0.2 V/-2.1 V	No	[52]
$PrPyrPbI_3$	10^5	10^4 s	2000	0.9 V/-1.2 V	No	[53]
$BnzPyrPbI_3$	10^4	N/A	N/A	0.9 V/-1.2 V	No	[53]
$(CH_3)_3SPbI_3$	10^2	10^3 s	300	0.2 V/-0.5 V	No	[54]
$CsCu_2I_3$	10^4	10^4 s	100	0.5 V/-0.5 V	Yes	[55]
K_2CuBr_3	10^5	10^3 s	200	0.27 V/-0.3 V	Yes	This work

Ag electrode and examined its RS performance, as filament-type RS devices are much less dependent on the electrode area. As shown in Figure S10 (Supporting Information), the switching performance difference between large and small Ag TE devices is insignificant, which supports the conductive filament as the RS mechanism. To further verify that the conductive filament is based on Ag ions, a device replacing the electrochemically active Ag TE with inert metal Au is made. As shown in Figure S11 (Supporting Information), the Au/K_2CuBr_3/ITO device only shows a certain degree of *I*–*V* hysteresis without significant RS phenomena. These results suggest that despite some mobile halide ions/vacancies existing in K_2CuBr_3 and contributing to RS, they are insufficient to form a conductive filament, highlighting the critical role of the Ag top electrode in inducing the observed resistive switching in our study.

To further study the switching mechanism of this device during RS, an *I*–*V* logarithm plot is made, along with the linear fitting for the HRS and LRS regions, respectively (Figure 4e). In the HRS region, at a low voltage below 0.1 V, the charge carrier experiences an interfacial Schottky barrier, resulting in a small slope of 0.25. When the voltage is between 0.1 and 0.2 V, the slope of the fitting line becomes 0.88, indicating that the *I*–*V* relationship follows the ohmic law ($I \propto V$). When voltage exceeds 0.2 V, the slope of the fitting line becomes 2.10, indicating the conduction mechanism transferred into space charge limited current (SCLC) conduction, with an *I*–*V* relationship of $I \propto V^2$.[50,51] When the device is set to LRS, only one linear region is observed and the slope is 1.06, denoting the ohmic law of conduction in LRS as a consequence of the formation of conductive filament.

The data retention ability of the device was studied by recording its current over time under a read voltage of 0.08 V when the device is set to LRS and HRS, respectively. As shown in Figure 4f, for both LRS and HRS, the device can maintain its performance for 1000 s without obvious fluctuation, together with a large On/Off storage window of 10^5, the non-volatile K_2CuBr_3 device provides excellent signal-to-noise ratio and stability for memory application. To investigate the endurance of the device, cyclic testing was carried out, as shown in Figure 4g. The device is repeatedly set to LRS and HRS for 200 cycles and the current in each state is recorded under a reading voltage of 0.08 V. One can see that the device can maintain the excellent On/Off ratio of 10^5 during the 200 cycles endurance test, which demonstrates a good reliability of this device. **Table 1** summarizes the performance of RS devices based on different 1D halide perovskites reported in the literature and this work.[24,52–55] The studied K_2CuBr_3 RS device exhibits a decent performance comparable with up-to-date lead-based perovskite devices and outperforms other lead-free perovskite counterpart in terms of On/Off ratio, cycling endurance, and much smaller set/reset voltage, representing the advantage in energy consumption. The widely available and non-toxic elemental composition of K_2CuBr_3, combined with its superior RS performance and cost-effectiveness, makes it an environmentally friendly candidate that merits further research for advanced RS applications.

The K_2CuBr_3 devices also demonstrate multi-level storage capability, which can be achieved by adjusting the compliance current during the SET process. Modulating the compliance current, defined as the maximum current allowed during *I*–*V* measurements, is a common technique to fine-tune resistive memory properties by directly tailoring the LRS value and the strength of the conducting filament. In our experiment, a consistent voltage sweep of 0 V → 0.4 V → -0.4 V → 0 V was applied, with compliance currents set at 10^{-4} A, 10^{-5} A, and 10^{-6} A, respectively, resulting in three distinct levels of LRS in the K_2CuBr_3 device, as illustrated in Figure 4h. The multi-level switching capability shown here significantly enhances data storage density, suggesting that the device may be suitable for a broader range of applications. It is worth noting that when the compliance current is excessively high (10^{-3}A), the HRS current of the device may progressively increase during subsequent sweeping cycles (Figure S12, Supporting Information). This phenomenon suggests that the conductive filament may become excessively robust, which consequently increases the difficulty of the RESET process. As a result, the On/Off ratio tends to decrease gradually. Since halide perovskites are sensitive to moisture and oxygen, the device may degrade over time when exposed to ambient air. As shown in Figure S13 (Supporting Information), the On/Off ratio gradually reduced from 10^5 to 10^1 after being stored in the air for 7 days. Similar to the advancements made in perovskite solar cells, it is worth more future research efforts in surface passivation and device encapsulation to improve the stability of perovskite-based RS devices.

Besides the memory application, perovskite-based RS devices are also ideal candidates for artificial synapses to transmit information. In a biological synapse, as shown in **Figure 5a**, when a signal is transmitted from the presynaptic neuron to the postsynaptic neuron, neurotransmitters like Ca^{2+} ions are released by the synaptic vesicle, diffuse through the cleft between axon and dendrite, and detected by the receptor.[56] For our RS artificial synapses, the top silver electrode and bottom ITO electrode represent the presynaptic and postsynaptic neurons, and the K_2CuBr_3 switching layer acts as the synaptic cleft with inspiration from the

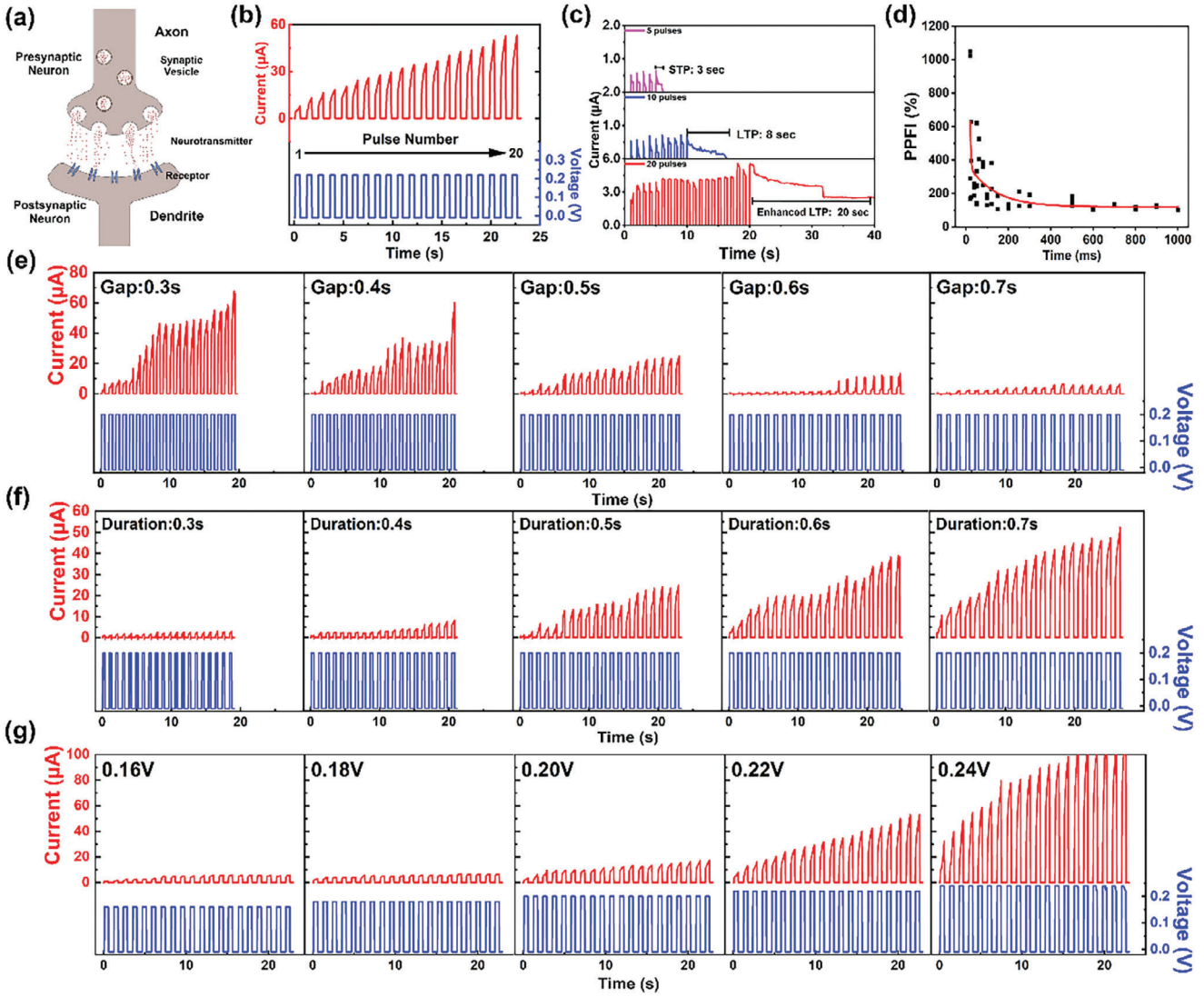

Figure 5. a) Schematic diagram demonstrating the principle of synapse behavior. b) The synaptic current of K_2CuBr_3 synapse with increasing pulse number (total number N = 20). c) STP and LTP behavior of the synapse device. d) PPF index as a function of pulse interval of the K_2CuBr_3 device. e) SRDP of K_2CuBr_3 device, pulse gap: 0.3-0.7 s. f) SDDP of K_2CuBr_3 device, pulse duration:0.3-0.7 s g) SIDP of K_2CuBr_3 device, pulse amplitude: 0.16–0.24 V.

biological synapse. In such devices, the migration of Ag ions and the formation of conductive filament represents the transportation of neuron transmitter.

Synaptic plasticity, the change in synaptic weight in response to activity spikes, defines the connection strength between pre-neurons and post-neurons and is crucial for human brain learning and memorization. In this work, the K_2CuBr_3 artificial synapses can also mimic a series of vital synaptic plasticity functions. In the study of SNDP, as shown in Figure 5b, the device current gradually increases with pulse number from 1 to 20 under constant amplitude, frequency, and pulse width (0.22 V, 600-ms pulse gap, 500-ms pulse width), indicating that the synaptic weight of K_2CuBr_3 synapse can be meticulously regulated. The STP and LTP functions are also studied by controlling different input pulse numbers (Figure 5c). The excitatory postsynaptic current (EPSC) is recorded when applying the pulse train (0.2 V amplitude, 500 ms duration, and 500 ms gap between each pulse) to the device. One can see that the K_2CuBr_3 synapse demonstrates STP after 5 pulses, with a sharp decrease in the current value within 3 s after the pulse train is stopped. Increasing the number of pulses to 10 further increases the potentiation to more than 8s, and an enhanced LTP is recorded with 20 pulses, in which the current value remains at a high level for more than 20 s. The synaptic plasticity is closely related to the number of pulse training sessions, mirroring the human brain's ability to enhance long-term memory with increased training.

The synaptic plasticity of a synapse is highly dependent on the pulse frequency, duration, and amplitude, namely, the SRDP, SDDP, and SIDP characteristics. The SRDP is studied under 20 pulses with a constant amplitude of 0.2 V and a pulse width of 500 ms (Figure 5e). When the gap between each pulse decreases from 700 to 300 ms, the current rises more rapidly, resulting in

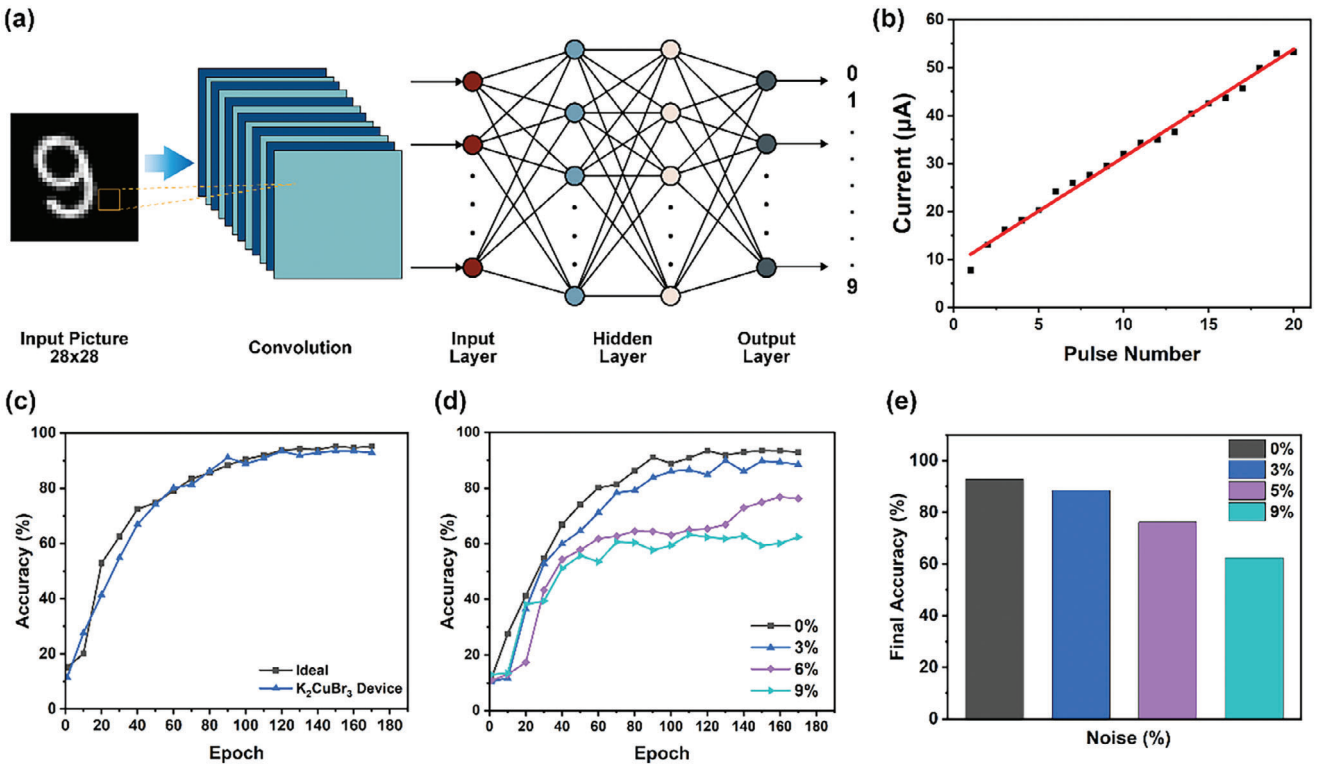

Figure 6. a) Schematic illustration of ANN image recognition. b) Potentiation of K_2CuBr_3 synapse devices as a function of pulse number (pulse amplitude: 0.22 V, duration: 500 ms, pulse gap: 600 ms). c) The recognition accuracy of K_2CuBr_3 neuromorphic devices compared to ideal devices. d) The recognition accuracy of K_2CuBr_3 neuromorphic devices under different proportions of noise pixels. e) Final achieved recognition accuracy under different noise ratios.

a substantial increase in the maximum current flowing through the device from 5 to 60 μA, a twelvefold increase, and thus demonstrating an enhanced potentiation with increased frequency of pulse interval. The pair-pulse facilitation (PPF) phenomenon is also observed during the study of SRDP. The PPF index (PPFI) is described by the ratio of the current amplitude of the second pulse to the first pulse ($I_2/I_1 \times 100\%$), which is dependent on the time interval between the two pulses, as illustrated in Figure 5d. The relationship between PPFI and time follows a double exponential function:[57]

$$\mathrm{PPFI}\,(\%) = C_1 e^{-\frac{t}{\tau_1}} + C_2 e^{-\frac{t}{\tau_2}} + 1 \quad (4)$$

The fitting result is indicated by the red line in Figure 5d, with $\tau_1 = 3.06$ and $\tau_2 = 125$ ms, demonstrating a millisecond-level response of the artificial synapse, which is on a similar timescale to that of general biological synaptic behavior.

The SDDP is studied under 20 pulses with a constant amplitude of 0.2 V and a pulse gap of 400 ms (Figure 5f). Similar to SRDP, the maximum current read in SDDP is also increased by a magnitude, from μA level to 10 μA level, as the pulse duration increases from 300 to 700 ms. The SIDP is also investigated with pulse voltages set from 0.16 to 0.24 V, while pulse duration (500 ms) and pulse gap (600 ms) remain constant, as shown in Figure 5g. The current difference between the 0.16 V pulse train and the 0.22 V pulse train is over a magnitude, from μA level to ≈50 μA, and the 0.24 V pulse train drives the device to the compliance current of 0.1 mA. These experiments prove the device's capability to demonstrate basic synaptic functionality, including SRDP, SDDP, and SIDP. In addition to the potentiation, synaptic depression behavior was also observed when negative voltage pulses of -0.27 V were applied, with a pulse duration of 300 ms and an interval gap of 500 ms. As shown in Figure S14 (Supporting Information), the synaptic depression exhibits an exponential decay from 100 to 50 μA in 20 pulses.

To further explore the potential of this RS synaptic device in ANN systems, we conducted a multilayer perceptron (MLP) simulation focused on image recognition using a 28 × 28 matrix and 10 000 samples (**Figure 6a**). Figure 6b illustrates the synaptic plasticity dataset collected from the K_2CuBr_3 device that creates the ANN simulation model, with each point on the graph representing the end current of each pulse. As shown in Figure 6c, after 180 training epochs, this device reaches an accuracy of 93% in image recognition, which is slightly lower than the ideal accuracy of 95% generated by the simulation program. Figure 6d,e demonstrate the decline in recognition accuracy when noise pixels were introduced into simulations. With 3% of noise pixels, the recognition accuracy decreased to 88%, demonstrating a certain degree of anti-interference capability.

3. Conclusion

In summary, we have prepared a lead-free halide perovskite RS device based on 1D K_2CuBr_3 perovskite thin films. The properties

of K_2CuBr_3 and the associated device were studied by multiple characterization methods. The device demonstrates bipolar resistive switching with a remarkable On/Off ratio of 10^5, exhibiting decent stability and reliability. Besides, the potential of neuromorphic computing was investigated, with the device successfully emulating various synaptic behaviors, including STP/LTP, PPF, SNDP, SRDP, SDDP, and SIDP. A simulation of visual recognition ANN using this device reached 93% accuracy after 180 training epochs. Overall, the excellent RS properties, combined with its low cost and minimal environmental impact, make K_2CuBr_3 an attractive candidate for RS memory and neuromorphic computing applications.

4. Experimental Section

Synthesis of K_2CuBr_3 Precursor Powder: Copper bromide (CuBr, 99.99%) and potassium bromide (KBr, 99.9%) were purchased from Sigma–Aldrich, and all chemicals were used without further purification. The ITO/glass substrates were purchased from Zhuhai Kaivo Optoelectronic Technology Company and silver pellets used for electrode deposition were purchased from Nano Vaccum. The K_2CuBr_3 powder was synthesized in a vacuumed environment. First, 0.624 g KBr and 0.376 g CuBr (stoichiometric ratio 2:1) were mixed and ground with mortars and pestles. The mixture was then transferred into the tube furnace, heated to 210 °C with Δ10 °C min^{-1}, and kept for 24 h under a 10-torr inert gas environment. After that, the furnace was cooled down to room temperature. Repeat the grinding and heating process 2 times to get the K_2CuBr_3 powder.

Fabrication of Film and RS Device: The vacuum thermal evaporation method was used to fabricate the K_2CuBr_3 film. The synthesized powder was placed on the bottom of the vapor deposition chamber. The ITO glass, used as substrate and BE, was cleaned with acetone, ethanol, and deionized water in an ultrasonic cleaner for 15 min, followed by a 10 min plasma treatment for surface cleaning to increase the surface hydrophilicity. The cleaned substrates were then put into the thermal evaporation chamber and started the vacuum process for 24 h to reach a high vacuum condition (10^{-7} Pa). The precursor powder was first preheated with Δ10 °C min^{-1} to reach 200 °C, followed by Δ5 °C min^{-1} to reach 300 °C. K_2CuBr_3 vapor started to form at the temperature of 300 °C. Use 0.1 Å sec^{-1} deposition speed to form the first 50 nm to create a fine base of the film, followed by 0.3 Å sec^{-1} to deposit the rest of the film. The substrates are heated to 100 °C during the deposition process. After the deposition of K_2CuBr_3 film, wait for one day to let the vapor of K_2CuBr_3 being evacuated out, and then deposit the silver TEs on the film using a shadow mask to construct Ag/K_2CuBr_3/ITO MSM structure.

Characterizations and Performance Tests: XRD (Aries Benchtop) was used to characterize the crystal structure of K_2CuBr_3 with Cu Kα (λ = 1.5418 Å). The surface and the cross-section of the synthesized film were investigated by field emission SEM (Joule JSM-IT710HR). The surface roughness of the film was analyzed by AFM (Bruker Dimension ICON SPM). The chemical contents and properties were studied by XPS (Thermo scientific ESCLAB250Xi), PL (Edinburgh FS5 Spectrofluorometer, wavelength: 300 nm), and PLE (Perkin Elmer LS-55). The thermal stability was tested by TGA-DSC (NETZSCH STA 449 F1). The TGA ramp rate was set at 10 °C min^{-1} from 20 to 800 °C, and the DSC was set at a ramp rate of 10 °C min^{-1} from 20 to 300 °C, both were tested under a N_2 rich environment. UV–vis (Perkin Elmer Lambda 950) and UPS (Thermo scientific ESCLAB250Xi) were used to calculate the band gap, CBM, and VBM positions of the material. Lake Shore Cryotronics PS-100 probe station was used to test the RS performance of the device under room temperature and vacuumed conditions (10^{-5} Torr). It was connected with a Keithley 4200A-SCS analyzer to accomplish all RS-related tests. The pulse measurements were accomplished by connecting the probe station with a Keysight 2902A source meter.

Supporting Information

Supporting Information is available from the Wiley Online Library or from the author.

Acknowledgements

This work was financially supported by the Australian Research Council (DE240100179) and the UNSW Science Faculty Research Grant (PS71686).

Conflict of Interest

The authors declare no conflict of interest.

Data Availability Statement

The data that support the findings of this study are available from the corresponding author upon reasonable request.

Keywords

1D, artificial synapse, memory, perovskite, resistive switching

Received: October 23, 2024
Revised: December 5, 2024
Published online: February 25, 2025

[1] F. Zahoor, T. Z. Azni Zulkifli, F. A. Khanday, *Nanoscale Res. Lett.* **2020**, *15*, 90.
[2] F. Chen, S. Zhang, L. Hu, J. Fan, C. H. Lin, P. Guan, Y. Zhou, T. Wan, S. Peng, C. H. Wang, L. Wu, T. M. Furlong, N. Valanoor, D. Chu, *Adv. Funct. Mater.* **2023**, *33*, 2300266.
[3] J. H. Yoon, Z. Wang, K. M. Kim, H. Wu, V. Ravichandran, Q. Xia, C. S. Hwang, J. J. Yang, *Nat. Commun.* **2018**, *9*, 417.
[4] H. Patil, H. Kim, K. D. Kadam, S. Rehman, S. A. Patil, J. Aziz, T. D. Dongale, Z. A. Sheikh, M. K. Rahmani, M. F. Khan, D.-k. Kim, *ACS Appl. Mater. Interfaces* **2023**, *15*, 13238.
[5] F. Zeng, Y. Guo, W. Hu, Y. Tan, X. Zhang, J. Feng, X. Tang, *ACS Appl. Mater. Interfaces* **2020**, *12*, 23094.
[6] S. Ham, S. Choi, H. Cho, S. I. Na, G. Wang, *Adv. Funct. Mater.* **2019**, *29*, 1970031.
[7] Y. Fang, Q. Li, J. Meng, T. Wang, H. Zhu, Q. Q. Sun, D. W. Zhang, L. Chen, *Adv. Electron. Mater.* **2023**, *9*, 2300120.
[8] J. Chen, X.-C. Zhao, Y.-Q. Zhu, Z.-H. Wang, Z. Zhang, M.-Y. Sun, S. Wang, Y. Zhang, L. Han, X.-M. Wu, T.-L. Ren, *ACS Nano* **2024**, *18*, 581.
[9] X. Duan, Z. Cao, K. Gao, W. Yan, S. Sun, G. Zhou, Z. Wu, F. Ren, B. Sun, *Adv. Mater.* **2024**, *36*, 2310704.
[10] R. Gao, A. C. P. Jain, S. Pandya, Y. Dong, Y. Yuan, H. Zhou, L. R. Dedon, V. Thoréton, S. Saremi, R. Xu, A. Luo, T. Chen, V. Gopalan, E. Ertekin, J. Kilner, T. Ishihara, N. H. Perry, D. R. Trinkle, L. W. Martin, *Adv. Mater.* **2020**, *32*, 1905178.
[11] J. C. Pérez-Martínez, M. Berruet, C. Gonzales, S. Salehpour, A. Bahari, B. Arredondo, A. Guerrero, *Adv. Funct. Mater.* **2023**, *33*, 2305211.
[12] A. Younis, L. Hu, P. Sharma, C. H. Lin, Y. Mi, X. Guan, D. Zhang, Y. Wang, T. He, X. Liu, B. Shabbir, S. Huang, J. Seidel, T. Wu, *Adv. Funct. Mater.* **2020**, *30*, 2002948.
[13] G. S. H. Thien, M. Ab Rahman, B. K. Yap, N. M. L. Tan, Z. He, P.-L. Low, N. K. Devaraj, A. F. Ahmad Osman, Y.-K. Sin, K.-Y. Chan, *ACS Omega* **2022**, *7*, 39472.

[14] Z. Xiao, Z. Song, Y. Yan, *Adv. Mater.* **2019**, *31*, 1803792.
[15] P. R. Anandan, M. Nadeem, C.-H. Lin, S. Singh, X. Guan, J. Kim, S. Shahrokhi, M. Z. Rahaman, X. Geng, J.-K. Huang, H. Nguyen, H. Hu, P. Sharma, J. Seidel, X. Wang, T. Wu, *Appl. Phys. Rev.* **2023**, *10*, 041312.
[16] M. Abd Mutalib, N. Ahmad Ludin, N. A. A. Nik Ruzalman, V. Barrioz, S. Sepeai, M. A. Mat Teridi, M. S. Su'ait, M. A. Ibrahim, K. Sopian, *Mate. Renewable. Sustainable Energy* **2018**, *7*, 7.
[17] M. Shahbazi, H. Wang, *Sol. Energy* **2016**, *123*, 74.
[18] T. Leijtens, R. Prasanna, A. Gold-Parker, M. F. Toney, M. D. McGehee, *ACS Energy Lett.* **2017**, *2*, 2159.
[19] B. W. Zhang, C.-H. Lin, S. Nirantar, E. Q. Han, Y. Zhang, Z. Wang, M. Lyu, L. Wang, *Small Struct.* **2024**, *5*, 2300524.
[20] R. L. Z. Hoye, J. Hidalgo, R. A. Jagt, J. P. Correa-Baena, T. Fix, J. L. MacManus-Driscoll, *Adv. Energy Mater.* **2022**, *12*, 2100499.
[21] X. Guan, Z. Lei, X. Yu, C.-H. Lin, J.-K. Huang, C.-Y. Huang, L. Hu, F. Li, A. Vinu, J. Yi, T. Wu, *Small* **2022**, *18*, 2203311.
[22] S. Ge, X. Guan, Y. Wang, C. H. Lin, Y. Cui, Y. Huang, X. Zhang, R. Zhang, X. Yang, T. Wu, *Adv. Funct. Mater.* **2020**, *30*, 2002110.
[23] J.-M. Yang, S.-G. Kim, J.-Y. Seo, C. Cuhadar, D.-Y. Son, D. Lee, N.-G. Park, *Adv. Electron. Mater.* **2018**, *4*, 1800190.
[24] E.-S. Choi, J.-M. Yang, S.-G. Kim, C. Cuhadar, S.-Y. Kim, S. H. Kim, D. Lee, N.-G. Park, *Nanoscale* **2019**, *11*, 14455.
[25] R. M. Biefeld, *Mater. Res. Bull.* **1975**, *10*, 1151.
[26] K. Yamabayashi, K. Okazaki, D. Nakauchi, T. Kato, N. Kawaguchi, T. Yanagida, *Radiat. Phys. Chem.* **2024**, *214*, 111292.
[27] F. C. Loh, K. L. Tan, E. T. Kang, *Eur. Polym. J.* **1991**, *27*, 1055.
[28] B. J. Tufts, I. L. Abrahams, C. E. Caley, S. R. Lunt, G. M. Miskelly, M. J. Sailor, P. G. Santangelo, N. S. Lewis, A. L. Roe, K. O. Hodgson, *J. Am. Chem. Soc.* **1990**, *112*, 5123.
[29] B. V. Crist, *Surf. Sci. Spectra* **1992**, *1*, 292.
[30] M. Oku, *J. Electron Spectrosc. Relat. Phenom.* **1995**, *74*, 135.
[31] B. R. Strohmeier, *Surf. Sci. Spectra* **1994**, *3*, 175.
[32] R. Scheer, H. J. Lewerenz, *J. Vac. Sci. Technol., A* **1994**, *12*, 56.
[33] D. E. Fowler, D. C. Miller, *Surf. Sci. Spectra* **1992**, *1*, 381.
[34] H. Su, Y. Xie, S. Wan, B. Li, Y. Qian, *Solid State Ionics* **1999**, *123*, 319.
[35] T. D. Creason, T. M. McWhorter, Z. Bell, M.-H. Du, B. Saparov, *Chem. Mater* **2020**, *32*, 6197.
[36] S. Li, J. Luo, J. Liu, J. Tang, *J. Phys. Chem. Lett.* **2019**, *10*, 1999.
[37] H. Chen, J. M. Pina, F. Yuan, A. Johnston, D. Ma, Z. Li, X. Li, S. Hoogland, Z. Lu, E. H. Sargent, *J. Phys. Chem. Lett.* **2020**, *11*, 4326.
[38] M. Z. Rahaman, S. Ge, C.-H. Lin, Y. Cui, T. Wu, *Small Struct.* **2021**, *2*, 2000062.
[39] W. Gao, G. Niu, L. Yin, B. Yang, J.-H. Yuan, D. Zhang, K.-H. Xue, X. Miao, Q. Hu, X. Du, J. Tang, *ACS Appl. Electron. Mater.* **2020**, *2*, 2242.
[40] J. M. Frost, A. Walsh, *Acc. Chem. Res.* **2016**, *49*, 528.
[41] A. J. Neukirch, I. I. Abate, L. Zhou, W. Nie, H. Tsai, L. Pedesseau, J. Even, J. J. Crochet, A. D. Mohite, C. Katan, S. Tretiak, *J. Phys. Chem. Lett.* **2018**, *9*, 7130.
[42] A. Walsh, D. J. Payne, R. G. Egdell, G. W. Watson, *Chem. Soc. Rev.* **2011**, *40*, 4455.
[43] Y. Han, X. Cheng, B.-B. Cui, *Mater. Adv.* **2023**, *4*, 355.
[44] P. Makula, M. Pacia, W. Macyk, *J. Phys. Chem. Lett.* **2018**, *9*, 6814.
[45] G. Li, J. Song, J. Wu, Z. Song, X. Wang, W. Sun, L. Fan, J. Lin, M. Huang, Z. Lan, P. Gao, *ACS Energy Lett.* **2021**, *6*, 3614.
[46] L. Liu, Y. Ma, Y. Wang, Q. Ma, Z. Wang, Z. Yang, M. Wan, T. Mahmoudi, Y. B. Hahn, Y. Mai, *Nanomicro Lett.* **2023**, *15*, 117.
[47] Q. Sun, A. Sadhu, S. Lie, L. H. Wong, *Adv. Mater.* **2024**, *36*, 2402412.
[48] C.-H. Lin, L. Hu, X. Guan, J. Kim, C.-Y. Huang, J.-K. Huang, S. Singh, T. Wu, *Adv. Mater.* **2022**, *34*, 2108616.
[49] X. Guan, T. Wan, L. Hu, C.-H. Lin, J. Yang, J.-K. Huang, C.-Y. Huang, S. Shahrokhi, A. Younis, K. Ramadass, K. Liu, A. Vinu, J. Yi, D. Chu, T. Wu, *Adv. Funct. Mater.* **2022**, *32*, 2110975.
[50] J. Ouyang, *Emerging Resistive Switching Memories*, Springer, Berlin, New York **2016**.
[51] M. A. Lampert, *Phys. Rev.* **1956**, *103*, 1648.
[52] X. Song, H. Yin, Q. Chang, Y. Qian, C. Lyu, H. Min, X. Zong, C. Liu, Y. Fang, Z. Cheng, T. Qin, W. Huang, L. Wang, *Research.* **2021**, *2021*, 9760729.
[53] S. K. Vishwanath, B. Febriansyah, S. E. Ng, T. Das, J. Acharya, R. A. John, D. Sharma, P. A. Dananjaya, M. Jagadeeswararao, N. Tiwari, M. R. C. Kulkarni, W. S. Lew, S. Chakraborty, A. Basu, N. Mathews, *Mate. Horiz.* **2024**, *11*, 4519.
[54] J. Gong, S. Ji, J. Li, H. Wei, W. Mao, J. Hu, W. Huang, X. He, X. A. Li, L. Chu, *Sci. China Mater.* **2024**, *67*, 2848.
[55] F. Huang, S. Ge, R. Wei, J. He, X. Ma, J. Tao, Q. Lu, X. Mo, C. Wang, C. Pan, *ACS Appl. Mater. Interfaces* **2022**, *14*, 43474.
[56] L. Chua, G. C. Sirakoulis, A. Adamatzky, *Handbook of Memristor Networks*, Springer, Berlin, New York **2019**.
[57] R. S. Zucker, W. G. Regehr, *Annu. Rev. Physiol.* **2002**, *64*, 355.